Chemical Science

ROYAL SOCIETY OF CHEMISTRY

EDGE ARTICLE

View Article Online
View Journal | View Issue

Check for updates

Cite this: *Chem. Sci.*, 2021, **12**, 15253

All publication charges for this article have been paid for by the Royal Society of Chemistry

Received 2nd August 2021
Accepted 10th November 2021

DOI: 10.1039/d1sc04231a

rsc.li/chemical-science

Open Access Article. Published on 10 listopada 2021. Downloaded on 13.02.2026 15:21:50.
This article is licensed under a Creative Commons Attribution-NonCommercial 3.0 Unported Licence.

Redox-active zinc thiolates for low-cost aqueous rechargeable Zn-ion batteries†

Madison R. Tuttle,‡[a] Christopher Walter,‡[a] Emma Brackman,[a] Curtis E. Moore,[a] Matthew Espe,[b] Chris Rasik,[b] Paul Adams[b] and Shiyu Zhang *[a]

Aqueous zinc-ion batteries (AZIBs) are promising candidates for large-scale electrical energy storage due to the inexpensive, safe, and non-toxic nature of zinc. One key area that requires further development is electrode materials that store Zn^{2+} ions with high reversibility and fast kinetics. To determine the viability of low-cost organosulfur compounds as OEMs for AZIBs, we investigate how structural modification affects electrochemical performance in Zn-thiolate complexes **1** and **2**. Remarkably, modification of one thiolate in **1** to sulfide in **2** reduces the voltage hysteresis from 1.04 V to 0.15 V. While **1** exhibits negligible specific capacity due to the formation of insulating DMcT polymers, **2** delivers a capacity of 107 mA h g^{-1} with a primary discharge plateau at 1.1 V *vs.* Zn^{2+}/Zn. Spectroscopic studies of **2** suggest a Zn^{2+} and H^+ co-insertion mechanism with Zn^{2+} as the predominant charge carrier. Capacity fading in Zn-**2** cells likely results from the formation of (i) soluble H^+ insertion products and (ii) non-redox-active side products. Increasing electrolyte concentration and using a Nafion membrane significantly enhances the stability of **2** by suppressing H^+ insertion. Our findings provide insight into the molecular design strategies to reduce the polarization potential and improve the cycling stability of the thiolate/disulfide redox couple in aqueous battery systems.

Introduction

Increasing demand for electrical energy combined with mounting environmental concerns over the use of fossil fuels has spurred interest in generating electrical energy from renewable resources. Electrical energy production from wind, solar, and water sources is naturally intermittent; therefore, large-scale, low-cost energy storage systems are necessary to compensate for this variability.[1] Conventional electrical energy storage systems, such as non-aqueous Li-ion batteries, have high energy densities and long cycle lifetimes, but their application in grid-scale energy storage is limited by the low natural abundance of lithium resources and potential safety hazards of flammable organic electrolytes.[2,3] Ideally, future large-scale energy storage systems should move beyond Li-ion batteries toward more sustainable, safer alternatives.

Aqueous zinc-ion batteries (AZIBs) are considered one of the most promising candidates for large-scale energy storage due to (i) the low cost, high capacity (820 mA h g^{-1}), and low toxicity of the Zn anode, (ii) the high ionic conductivity and safety of aqueous electrolytes, and (iii) the ease of manufacturing due to the stability of the Zn anode to ambient conditions.[4,5] One of the key research areas for progressing AZIBs toward grid-scale electrical energy storage applications is the development of compatible cathode materials. The majority of reported AZIB cathodes are inorganic materials, *e.g.*, metal oxides, Prussian blue analogs, and others.[4–12] Many of these materials have rigid lattices that can impede reversible Zn^{2+} (de)insertion, resulting in poor electrochemical kinetics (*i.e.*, sluggish ion diffusion and charge transfer) or irreversible lattice deformation. In contrast, organic electrode materials (OEMs) often have flexible solid-state structures that can easily accommodate reversible (de) insertion of multivalent cations, *e.g.*, Zn^{2+} and Al^{3+}, through lattice reorganization.[8,13–16] Furthermore, OEMs are more sustainable and structurally diverse compared to inorganic cathode materials.

State-of-the-art OEMs are based on quinone/phenazine moieties in AZIBs (Fig. 1A), which are often expensive to purchase or synthesize, limiting their practical use in large-scale energy storage.[4,5,8,17–23] To address this issue, we are interested in exploring other redox-active organic compounds beyond quinones/phenazines for use as OEMs in AZIB applications. Organosulfur compounds are especially promising, as they are highly cost-effective. In particular, 2,5-dimercapto-1,3,4-thiadiazole (DMcT, Fig. 1A) is an exceptionally inexpensive organosulfur starting material ($0.86 per gram) for many antiwear/anticorrosion lubricant additives.[24] In Li-ion batteries,

[a]*Department of Chemistry and Biochemistry, The Ohio State University, 100 W. 18th Ave, Columbus, OH, 43210, USA. E-mail: zhang.8941@osu.edu*

[b]*Lubrizol Corporation, 29400 Lakeland Blvd, Wickliffe, OH, USA*

† Electronic supplementary information (ESI) available. CCDC 2095600. For ESI and crystallographic data in CIF or other electronic format see DOI: 10.1039/d1sc04231a

‡ Madison R. Tuttle and Christopher Walter contributed equally to this work.

© 2021 The Author(s). Published by the Royal Society of Chemistry

Open Access Article. Published on 10 listopada 2021. Downloaded on 13.02.2026 15:21:50.
This article is licensed under a Creative Commons Attribution-NonCommercial 3.0 Unported Licence.

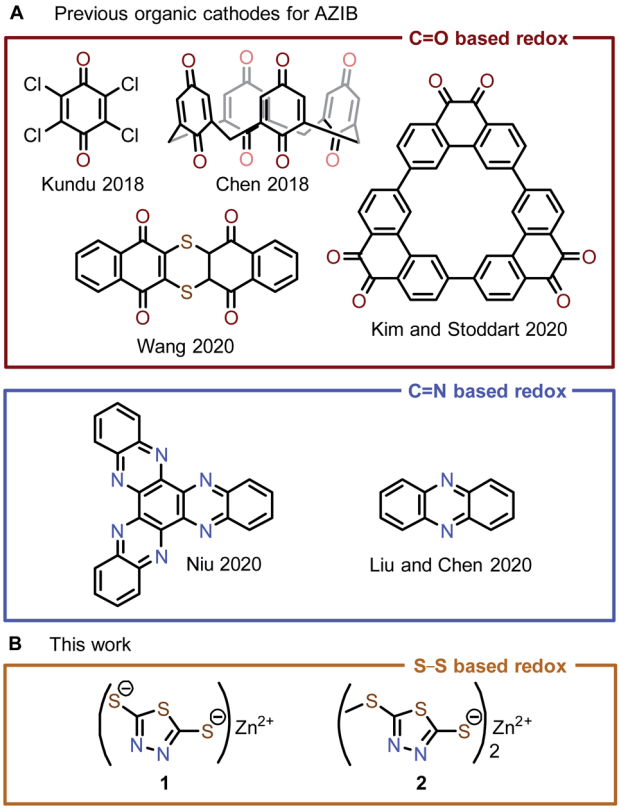

Fig. 1 (A) State-of-the-art organic cathode materials for AZIBs are mostly based on the redox of quinone/phenazine. (B) Zn-thiolate cathode materials reported in this work.

DMcT performs poorly as a cathode material due to the low conductivity and sluggish redox kinetics of disulfide-based electro(de)polymerization. As a result, Li-ion batteries with DMcT cathodes often require heating or the addition of electrocatalysts in order to achieve acceptable cycling performance.[25–29] Some modifications to DMcT have shown promise in improving its electrochemical behavior. For example, Buttry and coworkers found that deprotonation of the thiol moieties in DMcT and replacement of one thiol/thiolate moiety with a non-redox-active group produced more reversible redox behavior in non-aqueous electrolytes.[30] Furthermore, work by Oyama *et al.* showed that complexation with Lewis acidic metal ions like Cu^{2+} increases the conductivity of DMcT-based solid-state electrodes, facilitating DMcT electro(de)polymerization and improving electrode current densities.[31–33]

With the intention to fundamentally understand and improve the electrochemical behavior of DMcT for AZIB applications, we combine the benefits of previously established synthetic modifications and metal ion complexation in Zn^{2+}-DMcT complexes **1** and **2** (Fig. 1A). To determine how these structural modifications impact voltage polarization and cycle stability, we investigate the electrochemical performance of **1** and **2** as OEMs in AZIBs. Spectroscopic analysis coupled with pH-dependent studies of the best performing OEM **2** shows a predominantly Zn^{2+}-based (de)insertion mechanism followed by minor H^+ (de)insertion. The gradual capacity decay in Zn-**2** cells likely results from the formation of (i) soluble thiol 5-(methylthio)-1,3,4-thiadiazole-2-thiol (**4**) *via* H^+ insertion and (ii) non-redox-active 2,5-bis(methylthio)-1,3,4-thiadiazole (**5**) *via* a proposed redox-induced methyl shift reaction. Optimization of the Zn-**2** system with a concentrated Zn^{2+} electrolyte and a Nafion membrane inhibits H^+ insertion and significantly improves capacity retention. Our study illustrates the viability of the thiolate/disulfide redox couple in AZIBs and provides practical methods for optimizing the performance of organosulfur OEMs.

Result and discussion

Synthesis and characterization of DMcT derivatives 1–3

Zn complexes of 2,5-dimercapto-1,3,4-thiadiazole (**1**) and 5-(methylthio)-1,3,4-thiadiazole-2-thiol (**2**) were prepared by treating the corresponding potassium salts with an aqueous solution of $ZnCl_2$ (Fig. 2A).[34] The Zn-thiolate complexes form as easily isolable precipitates, and elemental analysis of complexes **1** and **2** is consistent with the corresponding empirical formulas (see ESI†). The solid-state structures of **1** and **2** were investigated by powder X-ray diffraction (PXRD). While the PXRD of **1** shows poor crystallinity (Fig. S4†), that of **2** exhibits many sharp diffraction peaks suitable for structure determination. The PXRD pattern of **2** indicates an I_4 space group with lattice parameters of $a = b = 18.137$ Å, $c = 8.710$ Å, and the diffraction pattern matches the simulated pattern obtained from the single-crystal X-ray diffraction data of **2** (Fig. S5†).[35] The crystal structure contains two Zn sites coordinated by either four N atoms (Zn–N distance: 2.036 Å) or four S atoms (Zn–S distance: 2.355 Å) in tetrahedral geometries. The ZnN_4 and ZnS_4 units are arranged alternately to afford a one-dimensional coordination polymer (Fig. 2B).

To elucidate the redox mechanism of **2**, the oxidation product of **2** was independently isolated by chemical oxidation with H_2O_2 to afford the corresponding disulfide (**3**) in 32% yield. Single crystals suitable for XRD analysis were obtained by slow evaporation of an ethyl acetate solution of **3**. Single-crystal XRD analysis shows molecules of **3** pack in a P_1 bar space group with lattice parameters of $a = 7.7086$, $b = 8.5728$, $c = 9.4538$, $\alpha = 85.498°$, $\beta = 86.274°$, $\gamma = 80.635°$ (Fig. 2C and S7†). Based on the unit cells of **2** and **3**, the removal of Zn^{2+} causes a *ca.* 14% volume contraction.

Solid-state cyclic voltammetry study

Compounds **1** and **2** feature similar thiolate functional groups that are expected to form disulfide bonds upon oxidation at 1.1–1.4 V *vs.* Zn^{2+}/Zn.[30–32] Compound **1** is known to undergo oxidation to form a mixture of dimers, oligomers, and polymers. Complete electropolymerization of **1** requires a total of two electrons per DMcT unit (Fig. 3A, top), affording a high theoretical capacity of 250 mA h g^{-1}. In contrast, compound **2** is unable to undergo electropolymerization since one redox-active thiolate is synthetically blocked. The oxidation of **2** generates disulfide **3** as the only product, affording a theoretical capacity of 136 mA h g^{-1} (Fig. 3A, bottom).

© 2021 The Author(s). Published by the Royal Society of Chemistry

Open Access Article. Published on 10 listopada 2021. Downloaded on 13.02.2026 15:21:50.
This article is licensed under a Creative Commons Attribution-NonCommercial 3.0 Unported Licence.

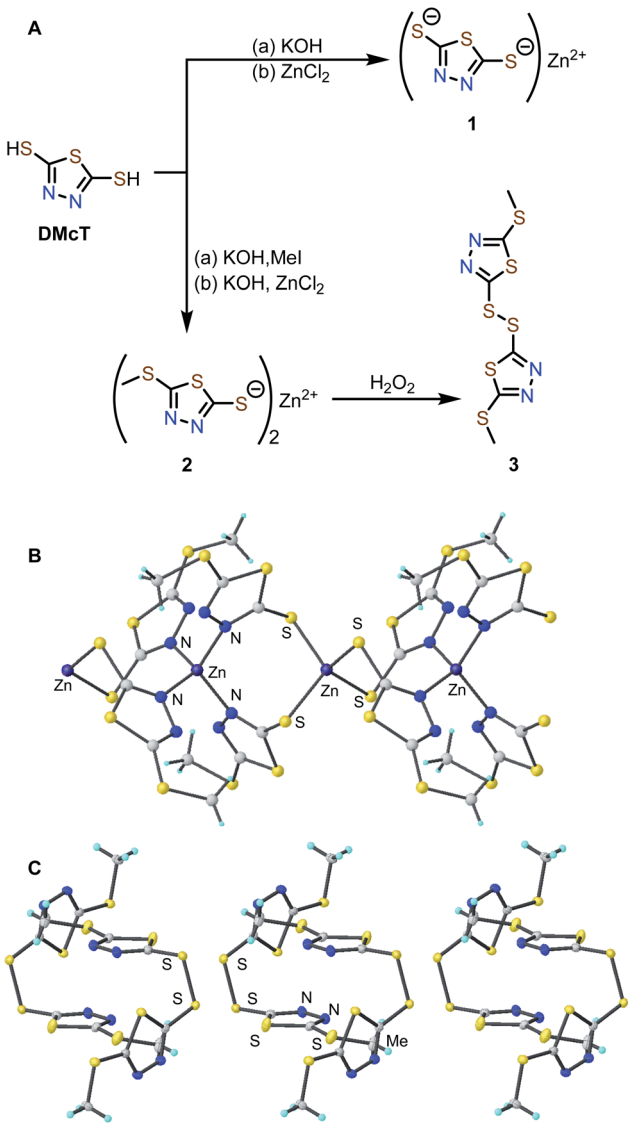

Fig. 2 (A) Synthesis of compounds **1**–**3**. Solid-state structure of (B) **2** and (C) **3** determined by powder and single-crystal XRD analysis. Atoms are color coded as followed: Zn: purple, S: yellow, N: blue, C: gray, H: aqua. The structure of **3** was rendered with thermal ellipsoids shown at a 50% level of probability.

The electrochemical properties of **1** and **2** in the solid-state were evaluated in coin-type cells with a Zn metal anode, Zn-thiolate cathode, and 1 M $ZnSO_4$ as the electrolyte. The solid-state CV of **1** shows a single oxidation peak at 1.43 V *vs.* Zn^{2+}/Zn (Fig. 3B), corresponding to the oxidation of **1** to a mixture of dimers, oligomers, and polymers. The reverse scan reveals two reduction peaks at 1.03 V and 0.42 V (Fig. 3B), which are assigned to the reduction of DMcT dimer and DMcT oligomer/polymer, respectively.[27–31,36] The 1.01 V redox polarization of **1** indicates poor electrochemical kinetics, which renders **1** impractical for energy storage applications.

By comparison, the CV of **2** shows a broad oxidation peak at 1.45 V followed by a reduction peak at 1.01 V, suggesting **2** undergoes a simple thiolate/disulfide redox mechanism (Fig. 3C). As **2** can only form dimers upon electrochemical oxidation, the voltage hysteresis is significantly reduced by 0.57 V compared to **1**. In subsequent scans, the primary redox couple of **2** shifts anodically, and a second reduction peak gradually appears at 0.94 V (Fig. 3C, purple trace). This observation suggests that **2** has a more complex electrochemical mechanism, which will be discussed in detail below.

Preliminary galvanostatic cycling experiments

To elucidate how molecular modification affects the cycling performance of **1** and **2**, galvanostatic charge–discharge (GCD) experiments were performed at a rate of 0.5C (125 mA g^{-1} for **1**, 68 mA g^{-1} for **2**) with voltage cut-offs selected based on solid-state CV studies. Zn-**1** cells deliver initial capacities of only 66 mA h g^{-1}, corresponding to 26% of theoretical values (Fig. 3D and S9†). The cell capacity quickly fades to <5% after five cycles. Similar to the CV study, the GCD profile of **1** exhibits a charge plateau at *ca.* 1.42 V and a sloping discharge plateau at *ca.* 0.34 V with a high voltage hysteresis of 1.04 V (Fig. 3E and S9†). In contrast, Zn-**2** cells achieve a specific capacity of 116 mA h g^{-1}, which decays over 30 cycles to 72% of the initial capacity with an average coulombic efficiency of 97% (Fig. 3D and S10†). The Zn-**2** cells exhibit a single charge plateau at 1.26 V and a primary discharge plateau at 1.10 V with a small voltage hysteresis of 150 mV (Fig. 3E). Interestingly, a secondary discharge plateau can be seen at *ca.* 1.0 V (Fig. S10†), consistent with the appearance of a second peak in later CV scans.

Primary redox mechanism of 2 in AZIB

The emergence of a new reduction peak/plateau suggests the development of a secondary redox process, prompting further investigation into the redox mechanism of **2**. First, we utilized *ex situ* X-ray fluorescence spectroscopy (XRF) to quantify the amount of Zn in fully charged or discharged samples of **2**. After charging, the Zn content in **2** is reduced to <30% of pristine values (from 1035 to 289 counts per second, Fig. 4B green trace and S18†), indicating that most of the Zn^{2+} ions are extracted from the cathode material during oxidation. After discharging, the Zn content returns to pristine values (1046 counts per second, red trace), indicating Zn^{2+} insertion occurs during reduction. The significant variation of Zn content in the cathode material reveals that Zn^{2+} is a predominant charge carrier in thiolate/disulfide redox.

Raman spectroscopy was also performed on charged and discharged samples of **2** to identify the primary redox-active species during cycling (Fig. 4C). Upon charging, the Zn–S vibrational feature at 247 cm^{-1} disappears while a new S–S vibrational feature emerges at 488 cm^{-1}, indicating Zn^{2+} deinsertion and formation of disulfide **3**. The S–S vibrational assignment was confirmed using a pristine sample of **3**, prepared by chemical oxidation (Fig. S19†). Upon discharge, the Zn–S vibration returns while the S–S vibration disappears. The Raman spectrum of charged **2** was compared to that of $ZnSO_4$ to evaluate a potential SO_4^{2-} (de)insertion mechanism. The signature SO_4^{2-} Raman signals (1022, 1071, 1081 cm^{-1}) are not

Open Access Article. Published on 10 listopada 2021. Downloaded on 13.02.2026 15:21:50.
This article is licensed under a Creative Commons Attribution-NonCommercial 3.0 Unported Licence.

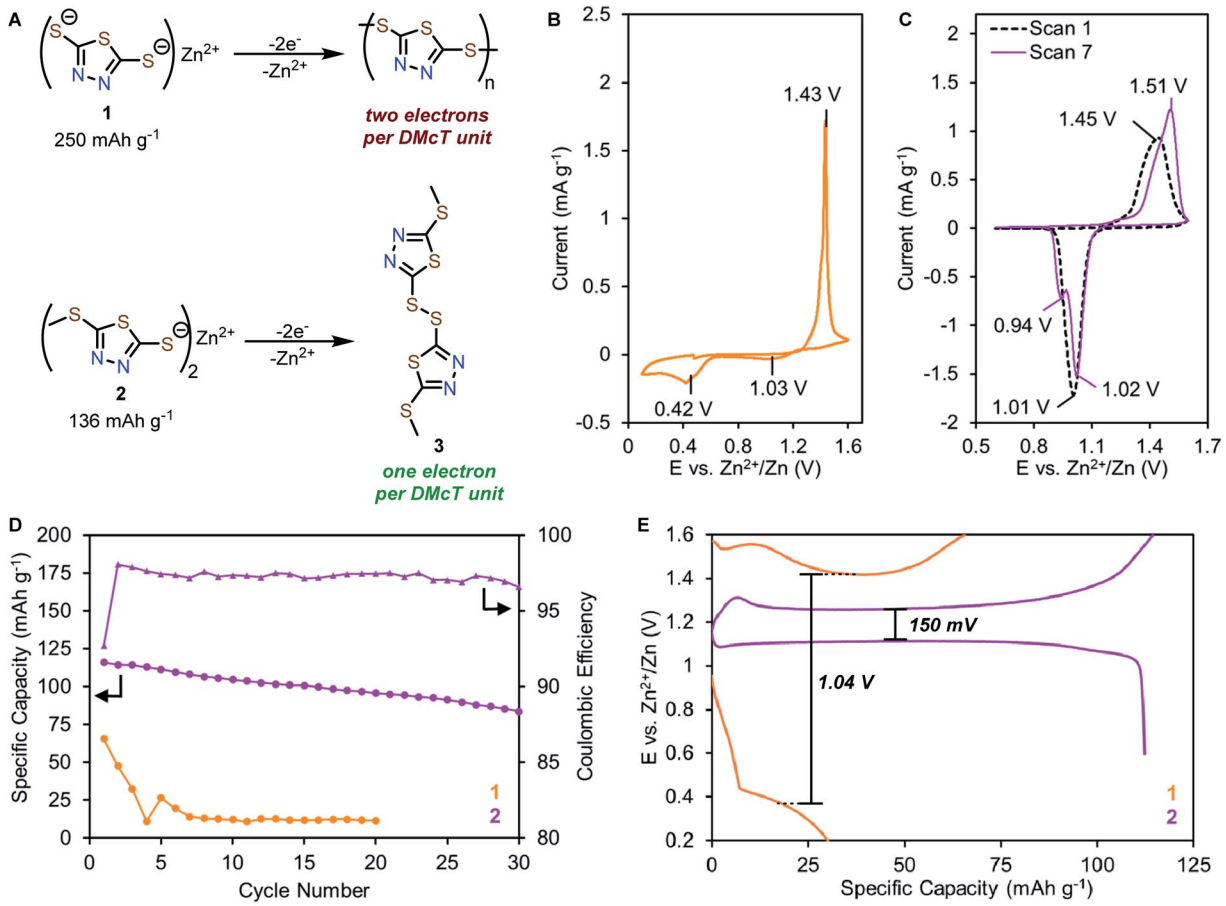

Fig. 3 (A) Oxidation of **1** and **2** to the corresponding disulfides. Solid-state CV measurements of coin cells with (B) **1** and (C) **2** as cathodes and 1 M $ZnSO_4$ aqueous electrolyte. Counter electrode: Zn. Scan rate: 0.1 mV s^{-1}. (D) Galvanostatic cycling comparison of **1** and **2** at a rate of 0.5C. (E) Typical galvanostatic charge–discharge cycling of **1** (orange), **2** (purple), and coulombic efficiency (purple triangle) of Zn-**2** cells.

observed in the charged sample, indicating that SO_4^{2-} does not participate as a charge carrier (Fig. S19 and 20†).

The Zn^{2+}-based (de)insertion mechanism was further verified by *ex situ* PXRD and SEM analysis (Fig. 4D, S5 and 6†). After the first cycle, charged **2** exhibits a PXRD pattern nearly identical to the pristine sample of disulfide **3**, while discharged **2** retains the PXRD pattern of pristine **2**. After 60 cycles, discharged **2** exhibits a slightly broader PXRD pattern compared to

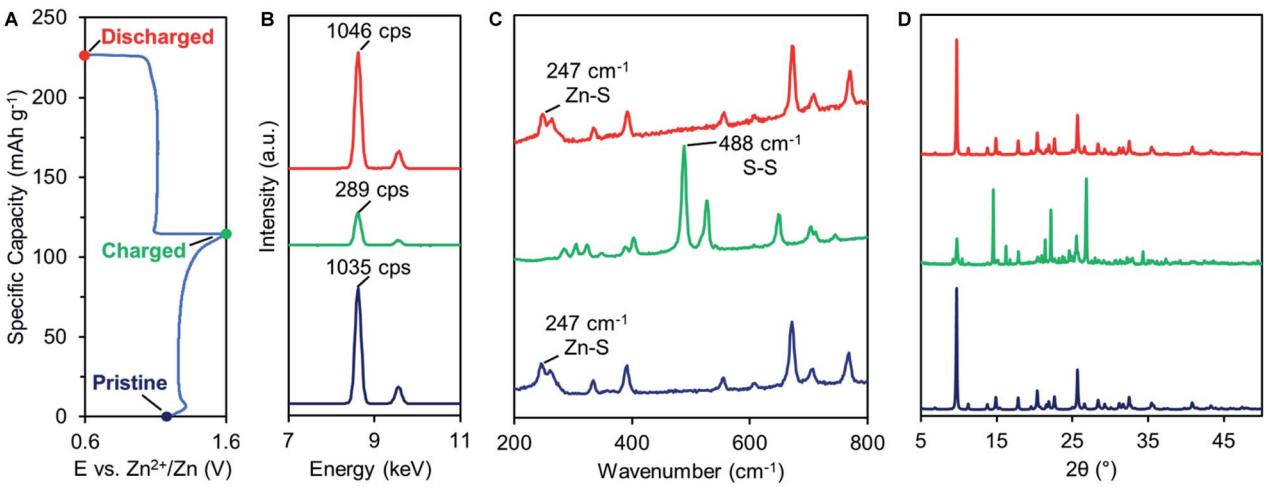

Fig. 4 (A) Typical GCD profile of **2**. *Ex situ* (B) XRF, (C) Raman, and (D) PXRD analysis of pristine (blue), charged (green), and discharged (red) **2**.

© 2021 The Author(s). Published by the Royal Society of Chemistry

Open Access Article. Published on 10 listopada 2021. Downloaded on 13.02.2026 15:21:50.
This article is licensed under a Creative Commons Attribution-NonCommercial 3.0 Unported Licence.

pristine **2** (Fig. S5†), suggesting a morphological change may have occurred during cycling. We utilized SEM to assess the morphology of pristine and cycled electrodes of **2**. Pristine **2** shows an irregular particle morphology that transforms into star-shaped crystals after 60 charge–discharge cycles (Fig. S6†). Morphology changes are common for organic electrode materials and are likely due to the disruption caused by ion insertion/desertion and volume change. Taken together, these studies suggest that the primary redox mechanism for **2** is the formation/breaking of the disulfide bond accompanied by Zn^{2+} (de)insertion (Fig. 5A, top). Given that Zn^{2+} is the predominant charge carrier, the discharge plateau at 1.10 V likely corresponds to Zn^{2+} insertion. However, understanding the mechanism of the secondary discharge plateau at 1.0 V could provide insight into the gradual capacity decay observed in Zn-**2** cells.

Evaluating proton (de)insertion mechanism in 2

While the most common and widely accepted AZIB mechanism involves the reversible (de)insertion of Zn^{2+}, co-insertion of Zn^{2+} and H^+ is also possible, as observed in many metal oxide cathode materials (*e.g.*, MnO_2, and $NaV_3O_8 \cdot 1.5H_2O$)[37–39] and recently in quinone- and phenazine-based OEMs.[22,40] Given the acidic nature of 1 M $ZnSO_4$ (pH 4.39), both Zn^{2+} and H^+ could potentially serve as charge carriers in the redox of **2**. Proton insertion should afford 5-(methylthio)-1,3,4-thiadiazole-2-thiol (**4**, Fig. 5A, bottom).

To evaluate a potential H^+ (de)insertion mechanism, three-electrode solid-state CV studies were performed using either 1 M $ZnSO_4$ or 1 M H_2SO_4 as the electrolyte. The working electrode was prepared with disulfide **3** to avoid biasing which ion was (de)inserted (Fig. 5A). The CV graph in 1 M H_2SO_4 is adjusted to pH = 4 based on the Nernst equation to represent the mildly acidic environment of 1 M $ZnSO_4$ (Fig. 5B and S8†). The first reduction peak in the solid-state CV of **2** in 1 M $ZnSO_4$ (pink trace) aligns with the reduction of **3** in 1 M $ZnSO_4$ (blue trace), confirming Zn^{2+} insertion (**3** to **2**) occurs at 1.03 V. Meanwhile, the second reduction peak in the solid-state CV of **2** (pink trace) aligns with the reduction of **3** in 1 M H_2SO_4 (red trace), suggesting H^+ insertion (**3** to **4**) occurs at 0.95 V. Furthermore, galvanostatic intermittent titration technique (GITT) was employed to determine the diffusion coefficients for each redox process (see ESI†). As Zn^{2+} is larger than H^+, the diffusion coefficient for Zn^{2+} insertion is expected to be slower than that of H^+ insertion.[38,41] The diffusion coefficients were determined to be 3.94×10^{-11} cm^2 s^{-1} for Zn^{2+} insertion (and 1.31×10^{-9} cm^2 s^{-1} for H^+ insertion (Fig. S13†). These CV and GITT experiments support the existence of a primary Zn^{2+} (de) insertion mechanism at *ca.* 1.0–1.1 V and a secondary H^+ (de) insertion mechanism at *ca.* 0.9–1.0 V.

To investigate the effects of H^+ insertion on the cycling stability of **2**, pH-dependent galvanostatic cycling studies were conducted using coin cells of **2** at 0.2C (27 mA g^{-1}). The degree of H^+ (de)insertion is expected to increase as the electrolyte becomes more acidic, leading to higher capacity contribution of the H^+ plateau. Interestingly, the capacity contribution due to H^+ insertion remains at *ca.* 20 mA h g^{-1} per cycle regardless of pH (Fig. S11†). Meanwhile, the overall capacity diminishes faster with lower coulombic efficiency as the concentration of H^+ increases (Fig. 5C). For example, Zn-**2** cells with pH = 4 electrolyte exhibit a 1.17% capacity loss per cycle and an average coulombic efficiency of 96.6%, while cells with pH = 1 electrolyte exhibit a 1.75% capacity loss per cycle and an average

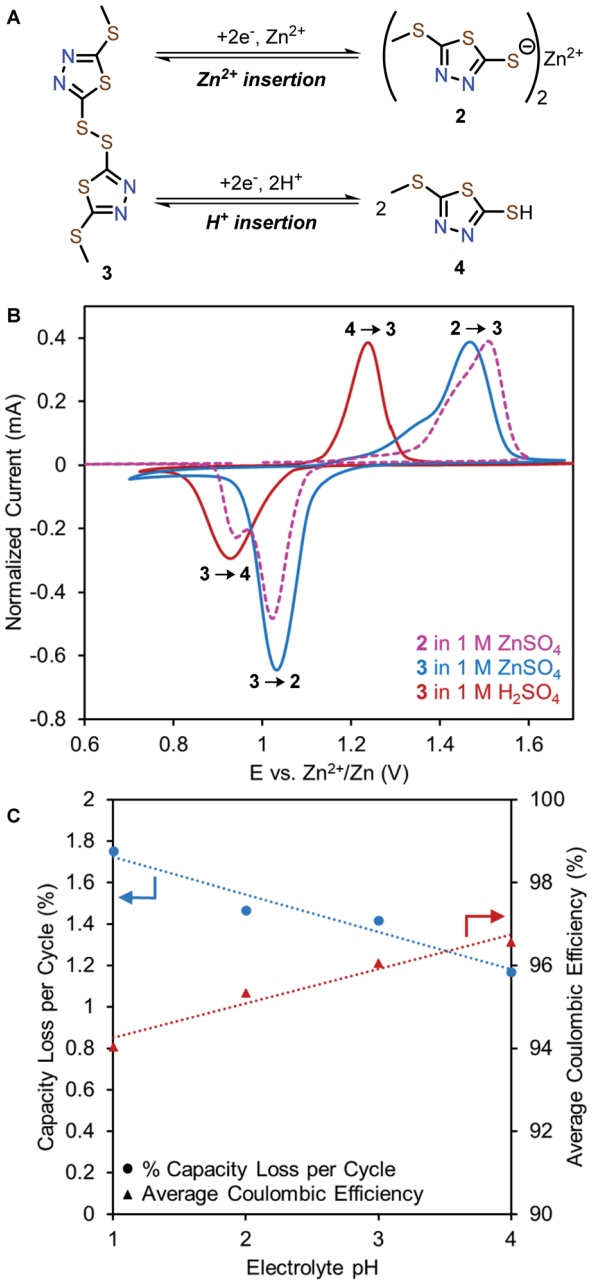

Fig. 5 (A) Possible Zn^{2+} and H^+ insertion products derived from reduction of **3**. (B) Solid state CV of **2** measured in a two-electrode cell with 1 M $ZnSO_4$ electrolyte (pink dotted line) and **3** measured in a three-electrode cell with 1 M $ZnSO_4$ (blue solid line) or 1 M H_2SO_4 electrolytes (red solid line). The position of the 1 M H_2SO_4 curve is adjusted to represent a dilute H_2SO_4 solution (pH = 4), calculated based on the Nernst equation. Current is normalized to oxidation peak for consistency. (C) pH-dependent capacity loss and coulombic efficiency of Zn-**2** cells.

Open Access Article. Published on 10 listopada 2021. Downloaded on 13.02.2026 15:21:50.
This article is licensed under a Creative Commons Attribution-NonCommercial 3.0 Unported Licence.

coulombic efficiency of 94.0% (Fig. 5C and S12†). Collectively, these experiments indicate that increasing the H^+ concentration of the electrolyte is detrimental to the cycling performance. We hypothesize this effect can be explained by the formation of **4** in acidic electrolytes, which could have a higher solubility than **2** due to its low molecular weight and hydrophilicity.[23]

Mechanism of capacity fading

The conversion of **2** to **4** can occur *via* two pathways (Scheme 1). Pathway 1 involves hydrolysis of **2** to afford **4**, which is a process that does not involve electrochemistry. Pathway 2 involves electrochemical conversion from **2** to **4** *via* **3**, which is consistent with the secondary discharge plateau at 1.0 V (*vide supra*). We found that **2** does not dissolve in protic solvents in any measurable quantity, likely due to its polymeric solid-state structure. Therefore, the formation of **4** *via* Pathway 1 is assumed to be negligible, leaving electrochemical Pathway 2 as the active mechanism for the conversion of **2** to **4.**

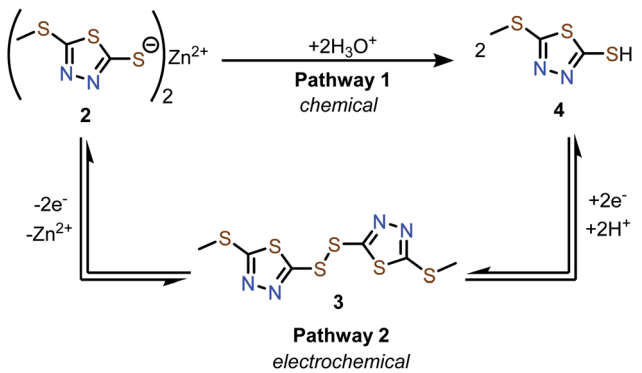

Scheme 1 Possible pathways for the conversion of **2** to **4** *via* chemical or electrochemical means.

Next, we evaluate the relative solubility of pristine samples of **3** and **4** in aqueous electrolytes using UV-vis spectroscopy. Stirring **3** and **4** in a 1 M $ZnSO_4$ solution for 30 minutes results in the formation of new bands around 306 and 297 nm, respectively, indicating the dissolution of **3** and **4** in the electrolyte (Fig. S22†). Assuming the same extinction coefficients in aqueous $ZnSO_4$ solutions and 1 M $Zn(OTf)_2$ in MeOH ($\varepsilon = 1.07 \times 10^4\ M^{-1}\ cm^{-1}$ for **3** and $1.02 \times 10^4\ M^{-1}\ cm^{-1}$ for **4**, Fig. S21–23†), the concentrations of **3** and **4** were calculated to be 0.044 mM and 7.7 mM, respectively (Fig. S22†). These experiments confirm that **4** is the most soluble redox-active species in aqueous electrolytes, and if formed, it can contribute to substantial capacity fading.

We propose a possible series of events that accounts for the capacity decay of **2** (Fig. 6A). Upon charging, Zn^{2+} deinserts from Zn-thiolate **2** to form disulfide **3.** Upon discharging, Zn^{2+} inserts to most interior thiolate sites. Since the terminal thiolate sites cannot provide a tetrahedral environment for Zn^{2+} to coordinate, these sites preferentially undergo H^+ insertion to form **4.** Because compound **4** has a higher solubility than other redox-active species, partial dissolution of **4** occurs during each

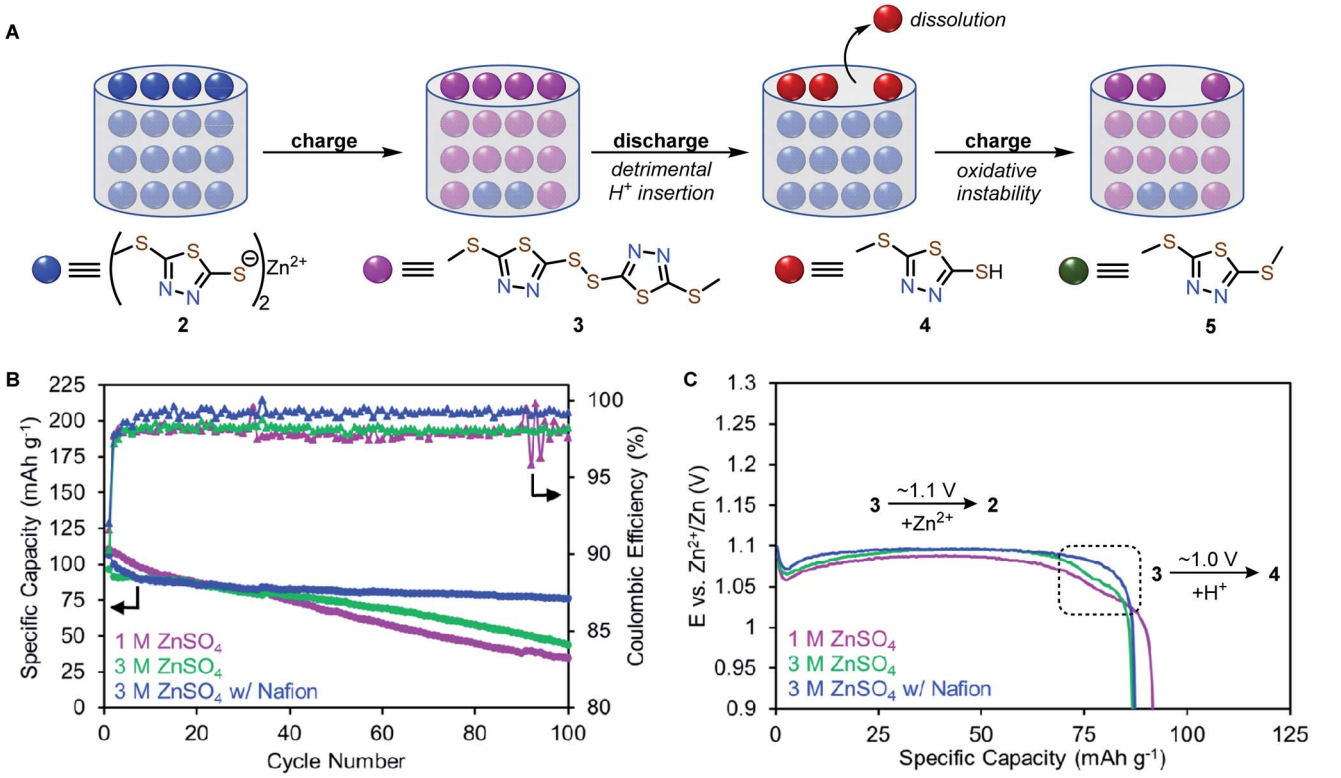

Fig. 6 (A) Qualitative illustration of the decomposition mechanism of **2**. (B) Long-term cycling stability and (C) galvanostatic discharge profile (cycle 10) of Zn-**2** cells in 1 M $ZnSO_4$ (purple), 3 M $ZnSO_4$ (green), and 3 M $ZnSO_4$ with Nafion (blue).

© 2021 The Author(s). Published by the Royal Society of Chemistry

Open Access Article. Published on 10 listopada 2021. Downloaded on 13.02.2026 15:21:50.
This article is licensed under a Creative Commons Attribution-NonCommercial 3.0 Unported Licence.

cycle, which is responsible for the capacity decay and low coulombic efficiency observed in Zn-**2** cells.

Mechanism-driven optimization of Zn-2 cells

We hypothesize that preventing the dissolution of **4** can improve the cycling stability of Zn-**2** cells. We found that the solubility of **4** is decreased by three-fold from 7.7 mM to 2.4 mM in 3 M $ZnSO_4$ (Fig. S22†). Galvanostatic cycling studies at a rate of 1C (136 mA g^{-1}) in 3 M $ZnSO_4$ show the capacity retention improves from 31% (in 1 M $ZnSO_4$) to 45% over 100 cycles and the average coulombic efficiency of **2** increases from 97.9% (in 1 M $ZnSO_4$) to 98.1%, and (Fig. 6B, S14 and 15†). The H^+ insertion plateau still exists at *ca.* 1.0 V in 3 M $ZnSO_4$, but the capacity contribution is reduced (10 mA h g^{-1}) compared to cells in 1 M $ZnSO_4$ electrolyte (20 mA h g^{-1}, Fig. 6C and S15†). The reduced proton insertion likely stems from a nearly two-fold increase of Zn^{2+} ions compared to H^+ (Table S3†).

Encouraged by the improved stability in 3 M $ZnSO_4$ electrolyte, we theorized that increasing the Zn^{2+} conductivity would further enhance cycling stability. The use of Nafion in AZIBs has been shown to enhance Zn^{2+} ion conductivity.[42,43] Indeed, coin cells of **2** with Nafion and 3 M $ZnSO_4$ electrolyte show the best cycling performance, achieving a specific capacity of 107 mA h g^{-1} with 71% capacity retention over 100 cycles and an average coulombic efficiency of 99% (Fig. 6B and S16†). Notably, the H^+ insertion plateau is absent in Zn-**2** cells with Nafion (Fig. 6C blue trace), suggesting that increasing Zn^{2+} ion conductivity suppresses H^+ insertion (Fig. 6C and S16†). Under the optimized conditions, variable-rate cycling studies of Zn-**2** cells shows capacities of *ca.* 75 mA h g^{-1} at 3C (408 mA g^{-1} Fig. S16†). While the cycling performance was significantly improved, Zn-**2** cells still exhibit a 0.4% capacity loss per cycle, perhaps due to the intrinsic chemical instability of **2** during cycling.

Chemical instability of 2

During post-mortem analysis of Zn-**2** cells, a noticeable stench was detected, indicating the formation of volatile S-containing compounds. Various cell components, *e.g.*, cathode and anode, were extracted with CH_2Cl_2 and analyzed by GC-MS (Fig. S24 and 25†). Both cathode and anode contain a decomposition product with m/z = 178, which can be assigned to dimethylated DMcT (**5**, Scheme 2). Since pristine **2** and **3** do not decay to **5** in the electrolyte, it is reasonable to hypothesize that formation of **5** is induced during thiolate/disulfide redox. Interestingly, methyl shifting has been observed for an analogous DMcT derivative (Scheme 2, top), which proceeds through a bimolecular transition state **TS**.[44] The formation of **5** could proceed through a similar transition state $\mathbf{TS_5}$, which involves the bimolecular interaction of two DMcTMe motifs (Scheme 2, bottom). In this case, a neutral (two radical DMcTMe motifs, n = 0) or monoanionic (one radical DMcTMe motif and one anionic DMcTMe motif, $n = {}^{\bullet}-$) transition state would be favored over a dianionic (two anionic DMcTMe motifs, n = 2−) transition state, as the coulombic repulsion between the two DMcTMe motifs would be significantly reduced. This could explain why

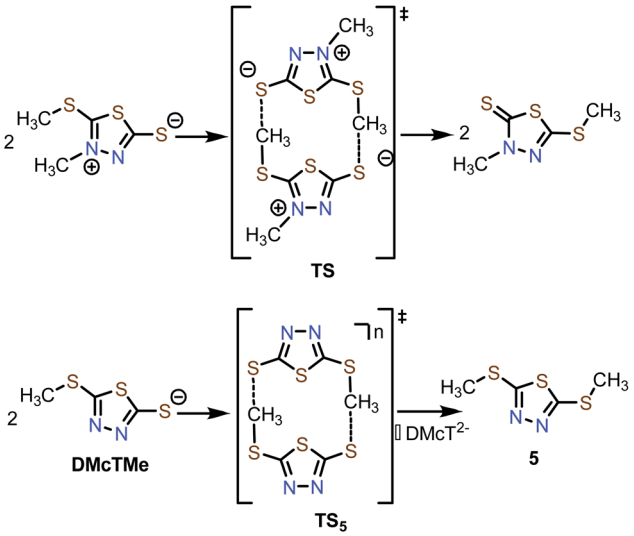

Scheme 2 Proposed mechanism for the decomposition of **2** to **5** during cycling.

decomposition to **5** is triggered by the oxidation of the DMcTMe anion (Fig. 6A). We are currently designing new Zn-thiolate complexes that would be more resilient toward such a methyl shift decomposition process.

Conclusion

In summary, our study describes the first application of a thiolate/disulfide-based redox mechanism in AZIBs. Electrochemical studies show that **1** exhibits irreversible electropolymerization, similar to parent DMcT, suggesting that complexation with Lewis acidic Zn^{2+} does little to improve electrochemical behavior. However, methylation of one thiolate group in **1** to sulfide in **2** leads to a significant reduction of voltage hysteresis from 1.04 V to 0.15 V, enabling the application of DMcT in AZIB. Investigation of the redox mechanism of **2** reveals that both Zn^{2+} and H^+ insertion occurs, but Zn^{2+} is the predominant charge carrier. Detailed spectroscopic studies indicate that capacity decay in Zn-**2** cells likely stems from the formation of (i) soluble thiol **4** *via* H^+ insertion and (ii) non-redox-active **5** *via* a proposed redox-induced methyl shift. Importantly, the formation and dissolution of **4** can be inhibited by high concentrations of Zn^{2+} and the use of a Nafion membrane. Our work highlights the importance of synthetic modification and mechanistic investigation as tools for systematically improving the electrochemical behavior of OEMs. Furthermore, our study demonstrates the viability of the thiolate/disulfide redox couple in AZIB applications, providing a new redox platform for the design of next-generation OEMs for sustainable energy storage.

Experimental section

All synthetic procedures were carried out under nitrogen (or argon) atmosphere using an MBraun glovebox and/or standard Schlenk techniques unless stated otherwise. ^1H and ^{13}C NMR spectra were recorded on Bruker 400 MHz spectrometer and were

Open Access Article. Published on 10 listopada 2021. Downloaded on 13.02.2026 15:21:50.
This article is licensed under a Creative Commons Attribution-NonCommercial 3.0 Unported Licence.

externally referenced to the NMR residual solvent peaks. ATR-IR spectra were measured using a Nicolet IR 200 with a diamond ATR accessory. The pH was measured using an Oakton pH 5+ handheld meter. Zn-thiolate cathode powders were prepared by milling a 70 : 20 : 10 mixture of active material, carbon black (Super P), and PVDF (polyvinylidene fluoride) binder, which was used directly in coin cell fabrication. Because the initial electrochemical behavior is known to be significantly different due to reorganization of the crystal lattice in OEMs,[45,46] we performed a single galvanostatic cycle at 0.5C (Fig. S9 and 10†) prior to cyclic voltammetry (CV) experiments. Cyclic voltammetry experiments were performed with a Biologic SP-150 single-channel potentiostat. Galvanostatic cycling experiments were performed with a LAND CT2001A battery testing system. Raman spectra were measured using a Renishaw Raman IR microprobe with a 514 nm laser beam. X-ray fluorescence (XRF) spectra were measured by an Olympus/Innov-X X-5000 XRF analyzer with a tantalum X-ray tube source and a silicon drift detector. Unless otherwise noted, all solvents were degassed and dried using a Pure Process Technology (PPT) solvent purification system and stored under an atmosphere of nitrogen over 4 Å molecular sieves. DMSO-d_6 (Cambridge Isotope Labs) was dried over CaH_2 and vacuum transferred onto 4 Å molecular sieves prior to use. $CDCl_3$ (Cambridge Isotope Labs) was degassed by three freeze–pump–thaw cycles and stored over 4 Å molecular sieves prior to use. All glassware were dried at 175 °C before use. All reagents were purchased from Sigma Aldrich unless otherwise noted.

Funding

This work was supported in part through Lubrizol Corporation, Ralph E. Powe Junior Faculty Enhancement Award by Oak Ridge Associated Universities, the National Science Foundation Graduate Research Fellowship under Grant No. DGE-1343012, the National Science Foundation under CBET-2124604, the Sustainability Institute at Ohio State University, and the Center for Emergent Materials, NSF MRSEC, under award number DMR-2011876.

Data availability

Crystallographic data for **3** has been deposited at the CCDC. Data for this paper, including experimental details, synthetic procedures, electrochemical details, crystallographic details, and Fig. S1–S25 are available at ESI.†

Author contributions

The manuscript was written by MRT, CW, and SZ. MRT and CW contributed equally. All authors have given approval to the final version of the manuscript.

Conflicts of interest

A provisional patent has been filed under the names of S. Z., M. R. T., C. R., and P. A. All other authors declare no competing interests.

Acknowledgements

The authors would like to the Wade and McGrier laboratories for ATR-IR, Dr Alicia Friedman for HRMS, Drs Tanya Whitmer and Dan Conroy for NMR, Tyler Weaver for XRF, and Dr Barbara Dunlap for Raman.

References

1 Z. Yang, J. Zhang, M. C. W. Kintner-Meyer, X. Lu, D. Choi, J. P. Lemmon and J. Liu, Electrochemical Energy Storage for Green Grid, *Chem. Rev.*, 2011, **111**, 3577–3613.
2 A. Manthiram, Materials Challenges and Opportunities of Lithium Ion Batteries, *J. Phys. Chem. Lett.*, 2011, **2**, 176–184.
3 A. Manthiram, An Outlook on Lithium Ion Battery Technology, *ACS Cent. Sci.*, 2017, **3**, 1063–1069.
4 L. Chen, Q. An and L. Mai, Recent Advances and Prospects of Cathode Materials for Rechargeable Aqueous Zinc-Ion Batteries, *Adv. Mater. Interfaces*, 2019, **6**, 1900387.
5 B. Tang, L. Shan, S. Liang and J. Zhou, Issues and Opportunities Facing Aqueous Zinc-Ion Batteries, *Energy Environ. Sci.*, 2019, **12**, 3288–3304.
6 Z. Rong, R. Malik, P. Canepa, G. Sai Gautam, M. Liu, A. Jain, K. Persson and G. Ceder, Materials Design Rules for Multivalent Ion Mobility in Intercalation Structures, *Chem. Mater.*, 2015, **27**, 6016–6021.
7 H. Glatz, E. Lizundia, F. Pacifico and D. Kundu, An Organic Cathode Based Dual-Ion Aqueous Zinc Battery Enabled by a Cellulose Membrane, *ACS Appl. Energy Mater.*, 2019, **2**, 1288–1294.
8 D. Kundu, P. Oberholzer, C. Glaros, A. Bouzid, E. Tervoort, A. Pasquarello and M. Niederberger, Organic Cathode for Aqueous Zn-Ion Batteries: Taming a Unique Phase Evolution toward Stable Electrochemical Cycling, *Chem. Mater.*, 2018, **30**, 3874–3881.
9 C. Xia, J. Guo, Y. Lei, H. Liang, C. Zhao and H. N. Alshareef, Rechargeable Aqueous Zinc-Ion Battery Based on Porous Framework Zinc Pyrovanadate Intercalation Cathode, *Adv. Mater.*, 2018, **30**, 1705580.
10 F. Ming, H. Liang, Y. Lei, S. Kandambeth, M. Eddaoudi and H. N. Alshareef, Layered $Mg_xV_2O_5 \cdot nH_2O$ as Cathode Material for High-Performance Aqueous Zinc Ion Batteries, *ACS Energy Lett.*, 2018, **3**, 2602–2609.
11 K. W. Nam, S. S. Park, R. dos Reis, V. P. Dravid, H. Kim, C. A. Mirkin and J. F. Stoddart, Conductive 2D Metal–Organic Framework for High-Performance Cathodes in Aqueous Rechargeable Zinc Batteries, *Nat. Commun.*, 2019, **10**, 4948.
12 Y. Ru, S. Zheng, H. Xue and H. Pang, Layered V-MOF Nanorods for Rechargeable Aqueous Zinc-Ion Batteries, *Mater. Today Chem.*, 2021, **21**, 100513.
13 M. Walter, K. V. Kravchyk, C. Böfer, R. Widmer and M. V. Kovalenko, Polypyrenes as High-Performance Cathode Materials for Aluminum Batteries, *Adv. Mater.*, 2018, **30**, 1705644.
14 B. Pan, J. Huang, Z. Feng, L. Zeng, M. He, L. Zhang, J. T. Vaughey, M. J. Bedzyk, P. Fenter, Z. Zhang,

© 2021 The Author(s). Published by the Royal Society of Chemistry

Open Access Article. Published on 10 listopada 2021. Downloaded on 13.02.2026 15:21:50.
This article is licensed under a Creative Commons Attribution-NonCommercial 3.0 Unported Licence.

A. K. Burrell and C. Liao, Polyanthraquinone-Based Organic Cathode for High-Performance Rechargeable Magnesium-Ion Batteries, *Adv. Energy Mater.*, 2016, **6**, 1600140.

15 I. A. Rodríguez-Pérez, Y. Yuan, C. Bommier, X. Wang, L. Ma, D. P. Leonard, M. M. Lerner, R. G. Carter, T. Wu, P. A. Greaney, J. Lu and X. Ji, Mg-Ion Battery Electrode: An Organic Solid's Herringbone Structure Squeezed upon Mg-Ion Insertion, *J. Am. Chem. Soc.*, 2017, **139**, 13031–13037.

16 D. J. Kim, D. J. Yoo, M. T. Otley, A. Prokofjevs, C. Pezzato, M. Owczarek, S. J. Lee, J. W. Choi and J. F. Stoddart, Rechargeable Aluminium Organic Batteries, *Nat. Energy*, 2019, **4**, 51–59.

17 Z. Guo, Y. Ma, X. Dong, J. Huang, Y. Wang and Y. Xia, An Environmentally Friendly and Flexible Aqueous Zinc Battery Using an Organic Cathode, *Angew. Chem., Int. Ed.*, 2018, **57**, 11737–11741.

18 G. Dawut, Y. Lu, L. Miao and J. Chen, High-Performance Rechargeable Aqueous Zn-Ion Batteries with a Poly(Benzoquinonyl Sulfide) Cathode, *Inorg. Chem. Front.*, 2018, **5**, 1391–1396.

19 Q. Zhao, W. Huang, Z. Luo, L. Liu, Y. Lu, Y. Li, L. Li, J. Hu, H. Ma and J. Chen, High-Capacity Aqueous Zinc Batteries Using Sustainable Quinone Electrodes, *Sci. Adv.*, 2018, **4**, eaao1761.

20 B. Häupler, C. Rössel, A. M. Schwenke, J. Winsberg, D. Schmidt, A. Wild and U. S. Schubert, Aqueous Zinc–Organic Polymer Battery with a High Rate Performance and Long Lifetime, *NPG Asia Mater.*, 2016, **8**, 283.

21 Y. Ma, X. Xie, R. Lv, B. Na, J. Ouyang and H. Liu, Nanostructured Polyaniline-Cellulose Papers for Solid-State Flexible Aqueous Zn-Ion Battery, *ACS Sustainable Chem. Eng.*, 2018, **6**, 8697–8703.

22 Z. Tie, L. Liu, S. Deng, D. Zhao and Z. Niu, Proton Insertion Chemistry of a Zinc–Organic Battery, *Angew. Chem., Int. Ed.*, 2020, **59**, 4920–4924.

23 Q. Wang, Y. Liu and P. Chen, Phenazine-Based Organic Cathode for Aqueous Zinc Secondary Batteries, *J. Power Sources*, 2020, **468**, 228401.

24 D.-P. Wei, L. Cao and L.-L. Wang, An Investigation into the Antiwear, Antioxidation, and Anticorrosion Behaviour of Some Derivatives of 2,5-Dimercapto-1,3,4-Thiadiaxole, *Lubr. Sci.*, 1995, **7**, 365–377.

25 Y. Liang, Z. Tao and J. Chen, Organic Electrode Materials for Rechargeable Lithium Batteries, *Adv. Energy Mater.*, 2012, **2**, 742–769.

26 M. Liu, S. J. Visco and L. C. De Jonghe, Electrode Kinetics of Organodisulfide Cathodes for Storage Batteries, *J. Electrochem. Soc.*, 1990, **137**, 750–759.

27 S. Picart and E. Geniès, Electrochemical Study of 2,5-Dimercapto-1,3,4-Thiadiazole in Acetonitrile, *J. Electroanal. Chem.*, 1996, **408**, 53–60.

28 N. Oyama, T. Tatsuma, T. Sato and T. Sotomura, Dimercaptan–Polyaniline Composite Electrodes for Lithium Batteries with High Energy Density, *Nature*, 1995, **373**, 598–600.

29 Y. Kiya, G. R. Hutchison, J. C. Henderson, T. Sarukawa, O. Hatozaki, N. Oyama and H. D. Abruña, Elucidation of the Redox Behavior of 2,5-Dimercapto-1,3,4-Thiadiazole (DMcT) at Poly(3,4-Ethylenedioxythiophene) (PEDOT)-Modified Electrodes and Application of the DMcT–PEDOT Composite Cathodes to Lithium/Lithium Ion Batteries, *Langmuir*, 2006, **22**, 10554–10563.

30 E. Shouji and D. A. Buttry, A Mechanistic Study of the Influence of Proton Transfer Processes on the Behavior of Thiol/Disulfide Redox Couples, *J. Phys. Chem. B*, 1999, **103**, 2239–2247.

31 N. Oyama, J. M. Pope and T. Sotomura, Effects of Adding Copper(ii) Salt to Organosulfur Cathodes for Rechargeable Lithium Batteries, *J. Electrochem. Soc.*, 1997, **144**, L47–L51.

32 T. Sotomura, T. Tatsuma and N. Oyama, An Organosulfur Polymer Cathode with a High Current Capability for Rechargeable Batteries, *J. Electrochem. Soc.*, 1996, **143**, 3152–3157.

33 N. Oyama and O. Hatozaki, New Composite Cathodes for Lithium Rechargeable Batteries, *Mol. Cryst. Liq. Cryst. Sci. Technol., Sect. A*, 2000, **349**, 329–334.

34 S. Shi, T. J. Katz, B. V. Yang and L. Liu, Use of Thiazyl Chlorides, Alkyl Carbamates, and Thionyl Chloride To Fuse 1,2,5-Thiadiazoles to Quinones and To Oxidize, Chlorinate, and Aminate Them, *J. Org. Chem.*, 1995, **60**, 1285–1297.

35 J. Zhang, X. Ma, W. Kong, F. Xie, S. Yuan, X. Song, Z. Lu and X. Xuan, A Sulfur Coordination Polymer with Wide Bandgap Semiconductivity Formed from Zinc(ii) and 5-Methyl-Sulfanyl-1,3,4-Thia-Diazole-2-Thione, *Acta Crystallogr., Sect. C: Struct. Chem.*, 2019, **75**, 1243–1249.

36 J. M. Pope, T. Sato, E. Shoji, N. Oyama, K. C. White and D. A. Buttry, Organosulfur/Conducting Polymer Composite Cathodes, *J. Electrochem. Soc.*, 2002, **149**, A939.

37 X. Jia, C. Liu, Z. G. Neale, J. Yang and G. Cao, Active Materials for Aqueous Zinc Ion Batteries: Synthesis, Crystal Structure, Morphology, and Electrochemistry, *Chem. Rev.*, 2020, **120**, 7795–7866.

38 W. Sun, F. Wang, S. Hou, C. Yang, X. Fan, Z. Ma, T. Gao, F. Han, R. Hu, M. Zhu and C. Wang, Zn/MnO_2 Battery Chemistry With H^+ and Zn^{2+} Coinsertion, *J. Am. Chem. Soc.*, 2017, **139**, 9775–9778.

39 F. Wan, L. Zhang, X. Dai, X. Wang, Z. Niu and J. Chen, Aqueous Rechargeable Zinc/Sodium Vanadate Batteries with Enhanced Performance from Simultaneous Insertion of Dual Carriers, *Nat. Commun.*, 2018, **9**, 1656.

40 Y. Wang, C. Wang, Z. Ni, Y. Gu, B. Wang, Z. Guo, Z. Wang, D. Bin, J. Ma and Y. Wang, Binding Zinc Ions by Carboxyl Groups from Adjacent Molecules toward Long-Life Aqueous Zinc–Organic Batteries, *Adv. Mater.*, 2020, **32**, 2000338.

41 T. Wu and W. Lin, Boosting Proton Storage in Layered Vanadium Oxides for Aqueous Zinc-ion Batteries, *Electrochim. Acta*, 2021, **394**, 139134.

42 M. Ghosh, V. Vijayakumar and S. Kurungot, Dendrite Growth Suppression by Zn^{2+}-Integrated Nafion Ionomer Membranes: Beyond Porous Separators toward Aqueous Zn/V_2O_5 Batteries with Extended Cycle Life, *Energy Technol.*, 2019, **7**, 1–10.

Open Access Article. Published on 10 listopada 2021. Downloaded on 13.02.2026 15:21:50.
This article is licensed under a Creative Commons Attribution-NonCommercial 3.0 Unported Licence.

43 M. Ghosh, V. Vijayakumar, B. Anothumakkool and S. Kurungot, Nafion Ionomer-Based Single Component Electrolytes for Aqueous Zn/MnO_2 Batteries with Long Cycle Life, *ACS Sustainable Chem. Eng.*, 2020, **8**, 5040–5049.

44 A. Espinosa, R. García, P. Molina and A. Tárraga, Unexpected Transalkylation on 3-Alkyl-2-Alkylthio-1,3,4-Thiadiazolium-5-Thiolates: A Computational and Experimental Mechanistic Study, *Org. Biomol. Chem.*, 2010, **8**, 1623–1628.

45 M. Lee, J. Hong, J. Lopez, Y. Sun, D. Feng, K. Lim, W. C. Chueh, M. F. Toney, Y. Cui and Z. Bao, High-Performance Sodium–Organic Battery by Realizing Four-Sodium Storage in Disodium Rhodizonate, *Nat. Energy*, 2017, **2**, 861–868.

46 Z. Wei, D. Wang, X. Yang, C. Wang, G. Chen and F. Du, From Crystalline to Amorphous: An Effective Avenue to Engineer High-Performance Electrode Materials for Sodium-Ion Batteries, *Adv. Mater. Interfaces*, 2018, **5**, 1800639.

© 2021 The Author(s). Published by the Royal Society of Chemistry